Research Square

Preprints are preliminary reports that have not undergone peer review.
They should not be considered conclusive, used to inform clinical practice,
or referenced by the media as validated information.

Desynchronization between CME Acceleration and Flare Reconnection

Anton Reva

reva.antoine@gmail.com

Space Research Institute

Ivan Loboda

Space Research Institute

Alexey Kirichenko

Space Research Institute

Sergey Bogachev

Space Research Institute

Research Article

Keywords:

Posted Date: November 4th, 2026

DOI: https://doi.org/10.21203/rs.3.rs-11060628/v1

License: This work is licensed under a Creative Commons Attribution 4.0 International License.
Read Full License

Additional Declarations: No competing interests reported.

Desynchronization between CME Acceleration and Flare Reconnection

Anton Reva[1] · **Ivan Loboda**[1] · **Alexey Kirichenko**[1] · **Sergey Bogachev**[1]

© **The author(s)** ●●●●

Abstract According to the standard coronal mass ejection (CME) model, both the flare and the CME are a result of the common process of magnetic reconnection. This implies that the CME impulsive acceleration and the flare reconnection should correlate in time. However, observations suggest that this correlation may break for CMEs associated with weak flares. In this work, we aim to find experimental evidence of such desynchronization. For this study, we chose a CME that 1) was associated with a weak B7.1 flare; 2) was continuously tracked from the solar surface up to the outer corona with high-cadence observations; 3) for which X-ray images were available. We measured the CME acceleration profile and compared it with the reconnection signatures: the derivative of the soft X-ray (SXR) emission and the motion of flare ribbons. The studied CME had non-trivial kinematics. It first impulsively accelerated to 440 km s^{-1} over $\approx$ 20 min, then decelerated to 280 km s^{-1} over $\approx$ 15 min, and then slowly accelerated up to 660 km s^{-1} over $\approx$ 2 h. We observed reconnection signatures only during the deceleration and second acceleration phases, suggesting that the main impulsive acceleration occurred without flare reconnection. We interpreted the first acceleration phase as a consequence of the kink instability. As the flux rope rose, it stretched the current sheet below it, which slowed down the CME. Eventually, the reconnection started inside the newly formed current sheet, and the CME started to accelerate again. These results show that CMEs can accelerate significantly without magnetic reconnection and exhibit a complex acceleration structure. This means that different mechanisms play a role in CME acceleration at different stages of its evolution.

Keywords: Coronal Mass Ejections, Initiation and Propagation; Prominences, Active; Flares, Dynamics

✉ Anton Reva
reva.antoine@gmail.com

[1] Space Research Institute, Profsoyuznaya 84/32, Moscow, 117997, Russia

1. Introduction

Coronal mass ejections (CMEs) are giant eruptions of plasma from the corona into interplanetary space. They are caused by the restructuring of the coronal magnetic field. The study of CMEs is important for solar physics (Chen 2011; Webb and Howard 2012) and the space weather science (Schwenn 2006; Pulkkinen 2007).

Since CMEs are often associated with flares (Andrews 2003; Yashiro et al. 2005; Reva et al. 2024), the standard CME model evolved as an extension of the standard flare model (CSHKP model: Carmichael 1964; Sturrock 1966; Hirayama 1974; Kopp and Pneuman 1976; Svestka and Cliver 1992). In the standard model, the CME pre-eruption configuration consists of a flux rope, a loop arcade below it, and a current sheet between the flux rope and an arcade. The flare begins with the onset of reconnection inside the current sheet. Reconnection accelerates electrons, which move down toward the chromosphere, where they stop, produce hard X-ray (HXR) emission, and heat plasma. The heated plasma fills the flare loops, producing flare soft X-ray (SXR) emission. At the same time, the upward reconnection outflow leads to the CME impulsive acceleration.

In the standard model, both the flare and the CME result from the same process of magnetic reconnection. Therefore, the CME impulsive acceleration should correlate in time with signatures of the magnetic reconnection. Indeed, researchers reported temporal correlations between CME impulsive acceleration and HXR emission (Temmer et al. 2008, 2010; Berkebile-Stoiser et al. 2012; Vievering et al. 2023), the rise of the SXR emission (Zhang et al. 2001, 2004; Gallagher, Lawrence, and Dennis 2003; Maričić et al. 2007; Bein et al. 2012), the flare ribbons' motions (Qiu et al. 2004; Jing et al. 2005; Zhu et al. 2020), and the appearance of the current sheet (Gopalswamy et al. 2018; Reva, Ulyanov, and Kuzin 2016; Reva et al. 2022).

The CME-flare connection can also be traced through statistics. Since the same magnetic reconnection fuels the CME and the flare, their energetic characteristics should correlate.

Indeed, for strong flares (M and X), such a correlation exists: the stronger the flare, the faster (on average) the CME (Yashiro et al. 2005; Vršnak, Sudar, and Ruzdjak 2005; Reva et al. 2024). However, for weak flares (C and below), this correlation breaks: CME speed does not depend on flare strength (Reva et al. 2024). Similarly, for fast CMEs, their speed correlates with the total magnetic flux reconnected during the flare, while for slow ones the correlation is absent (Zhu et al. 2020).

This pattern suggests that for strong flares, flare reconnection is a dominant mechanism for CME acceleration, while for weak ones, other mechanisms may play a bigger role. If this is true, then it is natural to assume that, for weak flares, we may observe a desynchronization between flare reconnection and CME acceleration.

The same conclusion could be drawn from the CME theory and magnetohydrodynamic (MHD) simulations. Flare reconnection is not the only mechanism that could lead to the CME eruption. CMEs could be initiated by ideal MHD instabilities – kink (Hood and Priest 1981) or torus (Kliem and Török 2006) –

without flare reconnection. The MHD simulations support this statement (Fan 2005; Inoue and Kusano 2006; Török and Kliem 2007; Rachmeler, DeForest, and Kankelborg 2009). However, these simulations show that during an eruption driven by an ideal MHD instability, a current sheet forms as a result of flux rope motion (Fan 2005; Inoue and Kusano 2006). Reconnection can occur inside this current sheet, leading to a weak flare. If the ideal MHD instability is the main driver of the CME acceleration, then there should be no CME-flare synchronization.

As we can see, statistics, MHD simulations, and the CME theory point in the same direction. For CMEs associated with weak flares, we may see a deviation from the standard CME model: desynchronization between CME impulsive acceleration and flare reconnection. Observing such an effect will provide experimental guidance for further development of the CME theory.

The progress in this area is mainly limited by the availability of experimental data. To comprehensively study CME kinematics, we need to continuously observe its evolution from the solar surface up to the far corona. The low corona ($r \lesssim 1.2\ R_\odot$) is well observed by EUV telescopes – e.g., *Atmospheric Imaging Assembly* (AIA: Lemen et al. 2012) – while the far corona ($r \gtrsim 2\ R_\odot$) is well observed by white-light coronagraphs: e.g., LASCO C2 and C3 (*Large Angle Spectroscopic Coronagraph*: Brueckner et al. 1995). However, the middle corona ($r \approx 1.2-2\ R_\odot$: West et al. 2023) is a 'blind zone' for traditional instruments, and it is not systematically observed. As a result, it is hard to accurately determine the timing of the CME acceleration.

Observations of the CME in the blind zone are relatively rare. They were observed by the LASCO/C1 coronagraph (Zhang et al. 2001), the *Siberian Solar Radio Telescope* (Alissandrakis et al. 2013), Mk4 coronameter (Bemporad et al. 2007; Reva et al. 2022) and *K-Coronameter* (K-Cor: Song et al. 2023) at the *Mauna Loa Solar Observatory* (MLSO), the *Full-disk EUV Telescopes* (FET: Reva et al. 2014; Reva, Ulyanov, and Kuzin 2016; Reva et al. 2016, 2017), the SPIRIT EUV telescope-coronagraph (*SPectroheliographIc X-Ray Imaging Telescope*: Slemzin et al. 2008), the *Sun Watcher with Active Pixels and Image Processing* (SWAP: Byrne et al. 2014; Mierla et al. 2013; D'Huys et al. 2017), the *Solar Ultraviolet Image* (SUVI: Seaton and Darnel 2018; Tadikonda et al. 2019), and *Extreme Ultraviolet Imager* (EUI: Mierla et al. 2022).

Among the instruments mentioned above, we want to point out the Mk4 and K-Cor coronameters. Because they are ground-based instruments, they cannot provide a 100% duty cycle. However, they cover the blind zone and observe the Sun routinely for many years. We think that their dataset is a good place to search for evidence of the CME-flare desynchronization.

In this work, we present observations of a CME associated with a weak flare that exhibited evidence of the CME-flare desynchronization. The event was observed with the Mk4 coronameter. As a result, we can continuously observe its evolution from the solar surface to the edge of the LASCO field of view. We will measure its kinematics and compare the timing of CME acceleration with signatures of flare reconnection.

Table 1. Instruments used in the research

Instrument	Field of View	Resolution	Cadence	Purpose
LASCO/C2	$2-6\ R_\odot$	$11''$	30 min	CME kinematics
LASCO/C3	$4-30\ R_\odot$	$56''$	60 min	CME kinematics
EIT	$\lesssim 1.2\ R_\odot$	$2.6''$	12 min	CME kinematics
				Ribbons' motion
Mk4	$1.14-2.86\ R_\odot$	$5.95''$	3 min	CME kinematics
PICS	$\leq 2.3\ R_\odot$	$2.9''$	3 min	CME kinematics
CHIP	$\leq 1.8\ R_\odot$	$2.3''$	3 min	CME kinematics
GOES-XRS	–	–	1 s	Flare dynamics
SXI	$\lesssim 1.2\ R_\odot$	$5''$	8 min	Flare dynamics
SPIRIT-Mg XII	$\lesssim 1.2\ R_\odot$	$8''$	2 min	Flare dynamics

2. Experimental Data

In this work, we study a CME that occurred on 2003 February 18. This event happened before the launch of the *Solar Dynamics Observatory* (SDO: Pesnell, Thompson, and Chamberlin 2012) and *Solar Orbiter* (SolO: Müller et al. 2020). That is why, instead of using data from modern, well-known observatories, we rely on a combination of obscure, older instruments.

The instruments used in this research fall into two groups. The first group measured CME kinematics, while the second observed the evolution of an associated flare. Table 1 summarizes the basic information about them. A more detailed description is given below.

2.1. Data for CME Kinematics

To comprehensively study the CME kinematics, we need to continuously observe its evolution from the solar surface up to the outer edge of coronagraphs' field of view. No existing instrument can do this alone. Additionally, to measure the fine structure of its acceleration, we need a high cadence. For these reasons, we need to combine all available data that observed the studied CME.

To study the outer corona, we use the *Large Angle Spectroscopic Coronagraph* (LASCO: Brueckner et al. 1995), which worked on board the *Solar and Heliospheric Observatory* (SoHO: Domingo, Fleck, and Poland 1995). LASCO is a set of white-light coronagraphs that observe the solar corona from 1.1 $R_\odot$ up to 30 $R_\odot$ (C1, $1.1-3\ R_\odot$; C2, $2-6\ R_\odot$; C3, $4-30\ R_\odot$). In 1998, LASCO C1 stopped working, and for this research, only C2 and C3 data are available. Coronagraph C2 has a resolution of $11''$, and C3 has a resolution of $56''$.

To study CMEs in the inner corona, extreme-ultraviolet (EUV) telescopes are usually used. In our research, we use the *Extreme ultraviolet Imaging Telescope* (EIT: Delaboudinière et al. 1995), which operated on board SoHO. EIT registered narrowband solar images at wavelengths centered at 171, 195, 285, and 304 Å. The instrument has a pixel size of $2.6''$ and a spatial resolution of $5''$. The EIT had two observational modes: synoptic and 'CME watch.' In synoptic

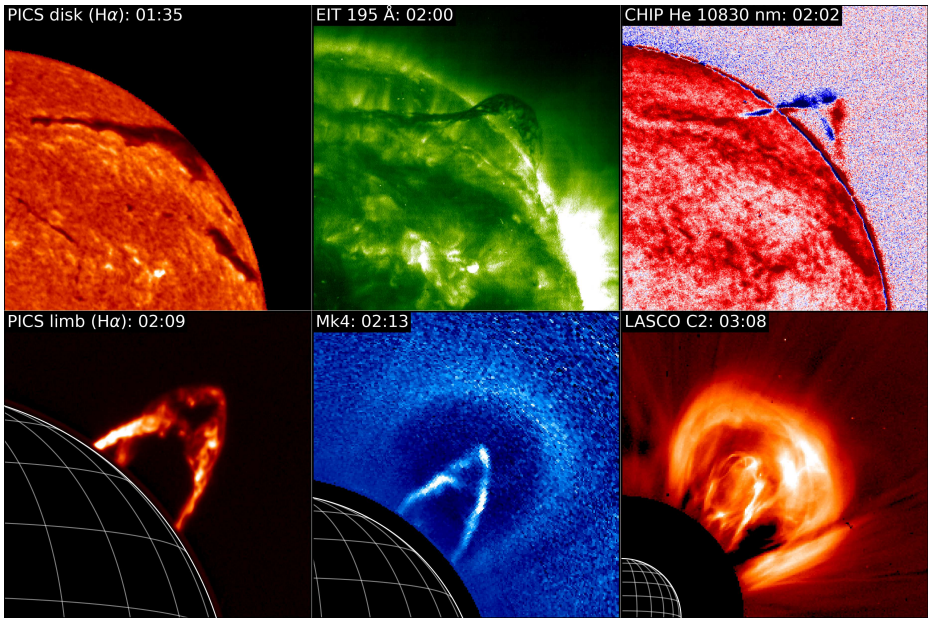


Figure 1. CME eruption. In the CHIP image, blue indicates positive values and red indicates negative values. PICS limb, Mk4, and LASCO images are base-difference images. All images were taken on 18 February 2003.

mode, it takes images in all four channels every 6 h. In the 'CME watch' mode, the telescope takes images in the 195 Å channel every 12 min.

Observations of the CME in the blind zone are covered by the Mk4 coronameter at *Mauna Loa Solar Observatory* (MLSO). Additionally, two other instruments at MLSO – *Polarimeter for Inner Coronal Studies* (PICS) and *Chromospheric Helium-I Imaging Photometer* (CHIP) – observed the studied event. They provide additional data points for kinematics measurements in the blind zone and low corona.

Mk4 coronameter (DOI: 10.5065/D66972C9; Elmore et al. 2003) built images of the solar corona from 1.14 to 2.86 $R_\odot$ in the white light (700–900 nm). It had a spatial resolution of 5.95″ and a cadence of 3 min.

PICS (DOI: 10.5065/D65719TR) registered Hα images (6563 Å) with a field of view of 2.3 $R_\odot$, a spatial resolution of 2.9″, and a cadence of 3 min. The instrument operated in two modes: limb observations and disk observations (see Figure 1). In limb mode, an artificial moon occulted the solar disk, which helps to observe prominence eruptions better. In disk mode, the solar disk is not occulted. The limb signal is still present in the images, but is less distinct than in limb mode.

CHIP (DOI: 10.5065/d6ww7gf7) built solar images at the He I 1083 nm line. The instrument had a field of view of ≈ 1.8 $R_\odot$, a cadence of 3 min, a pixel size of 2.3″, and a measured spatial resolution of $\approx 8''$.

The He I 1083 nm line image is produced by subtracting a line and a continuum exposure. Due to Doppler shifts, some of the pixels in the CHIP image will have

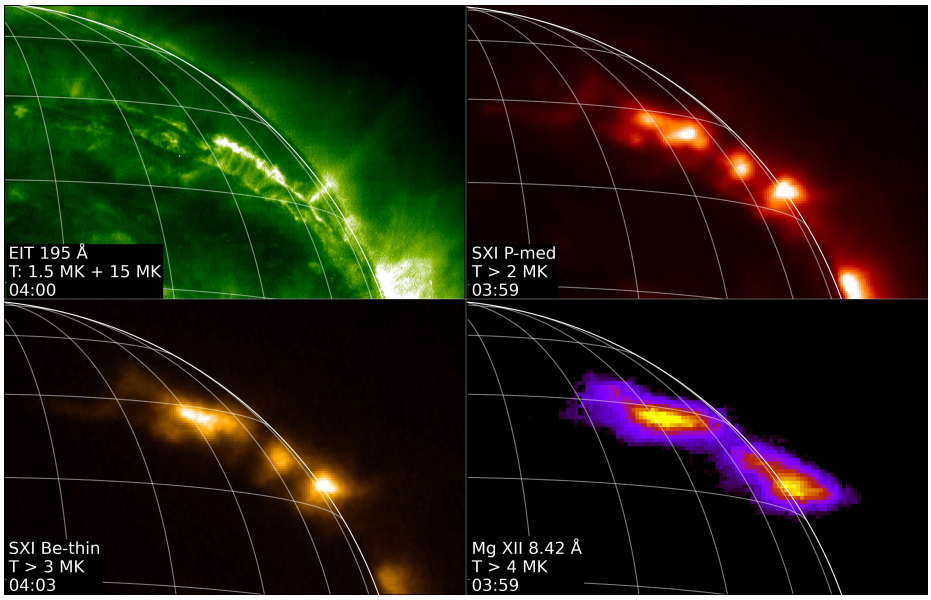


Figure 2. Flare arcade. Images were taken on 18 February 2003.

positive and some negative values (see Figure 1). In this research, we do not analyze the observed Doppler shifts and only use CHIP images to determine the position of an erupting prominence.

2.2. Data for Flare Dynamics

The widely used instrument for flare research is the *X-ray Sensor* (XRS) on board the *Geostationary Operational Environmental Satellite* (GOES: Hanser and Sellers 1996). XRS measures full-Sun integrated X-ray flux in two spectral channels: 1 – 8 Å and 0.5 – 4 Å. The flux in the 1 – 8 Å channel is commonly used to classify flare strength, and the rise in this channel is commonly used as a marker of flare onset.

The main disadvantage of GOES-XRS is the lack of imaging capabilities. Signals from different flares can overlap, which complicates diagnostics. For better flare analysis, X-ray images are desirable.

As an X-ray imager, we use the Mg XII spectroheliograph (Zhitnik et al. 2003a), which was a part of the SPIRIT complex (*SPectroheliographIc X-Ray Imaging Telescope*: Zhitnik et al. 2002, 2003b) on board the CORONAS-F satellite (*Complex Orbital Observations Near-Earth of Activity on the Sun*: Oraevsky and Sobelman 2002). The instrument built monochromatic images of the solar corona in the Mg XII 8.42 Å line. The main strength of the Mg XII spectroheliograph is its temperature selectivity. The Mg XII 8.42 Å line emits only at temperatures above 4 MK, making the instrument a useful tool to study heating processes in the solar corona (Urnov et al. 2007; Kirichenko and Bogachev 2017; Reva et al. 2018, 2023; Kirichenko et al. 2024). During the studied event, the Mg XII spectroheliograph had a cadence of 2 min and an angular resolution of

8″. For more technical details about the instrument, see Zhitnik et al. (2003a) and Reva et al. (2021).

The temperature selectivity of the Mg XII spectroheliograph is also its weakness. Since most of the solar corona has a temperature below 4 MK (Paterson et al. 2023; Ulyanov et al. 2024), most pixels in the Mg XII images have no signal (see Figure 2). It could be hard to interpret Mg XII images without any auxiliary data. To help interpret the Mg XII images, we use images from EIT and the *Solar X-ray Imager* (SXI).

The *Solar X-ray Imager* (SXI: Hill et al. 2005; Pizzo et al. 2005) worked on board the GOES-12 satellite. The telescope provided full-disk soft X-ray solar images in the 6 – 60 Å wavelength range with an angular resolution of ≈ 10″ and a 5″ pixel size. The 'Be-thin' channel of SXI is sensitive to the same temperatures as the Mg XII spectroheliograph but with a contribution from low-temperature background.

2.3. Data We did not Use

For flare diagnostics, HXR and radio emission data are commonly used. We checked the available data, but because the flare was weak, the existing instruments did not register any meaningful signal.

During the studied event, several HXR instruments were operating: *Reuven Ramaty High Energy Solar Spectroscopic Imager* (RHESSI: Lin et al. 2002), *Helicon*/CORONAS-F (Frederiks et al. 2007), IRIS/CORONAS-F (Dmitriev et al. 2006), and *Konus-Wind* (Aptekar et al. 1995). RHESSI and *Helicon* did not register HXR emission above the background during the studied period. IRIS and *Konus-Wind* had a data gap during the CME eruption.

As for the radio data, the Culgoora (Prestage et al. 1994) and Learmonth (Zhang et al. 2021) radio spectrographs observed the Sun during the studied period. However, they also did not register a signal above the background.

3. Results

3.1. General Description

In this work, we study a prominence eruption that occurred on 18 February 2003. The prominence was located in a north-western part of the Sun. It was ≈ 430 Mm long. Around 01:35 UT, the prominence lost equilibrium and started to erupt (see Figure 1). In white-light images, the CME had a classical three-part structure: a bright frontal loop, a dark cavity, and a bright core (Illing and Hundhausen 1985; Webb and Hundhausen 1987; Song et al. 2023).

The CME evolution was observed continuously with multiple instruments: PICS, EIT, CHIP, Mk4, and LASCO. This allows for a comprehensive study of its kinematics.

As the CME erupted, a weak B7.1 flare occurred below it (see Figures 2 and 3). The flare had a typical morphology: a flare arcade with flare ribbons and hot loop-top emission.

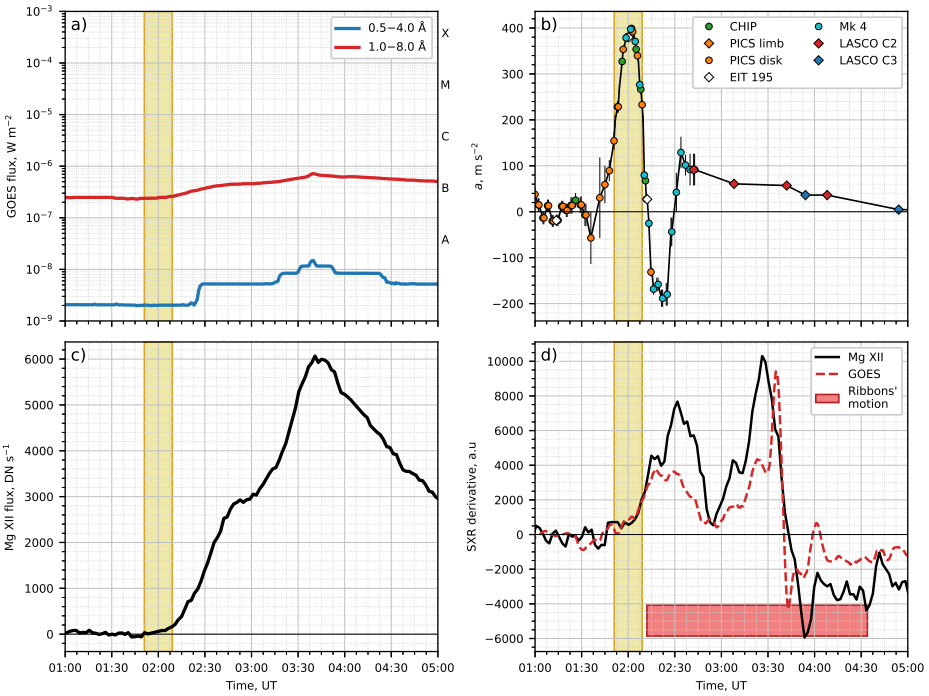


Figure 3. CME-flare timing. **a**) GOES flux. **b**) CME acceleration. **c**) Mg XII flux. **d**) Derivatives of the SXR flux: GOES (*red dashed line*) and Mg XII (*black line*). The *yellow vertical stripe* marks the CME's first acceleration phase. The *red horizontal stripe* marks the flare ribbons' motion.

As we see, the morphology of the studied event is consistent with the standard flare model: we observed a prominence eruption, a three-part CME structure, a rise in X-ray emission, a flare arcade, flare ribbons, and hot loop-top sources. However, some aspects of it looked suspicious to us.

First, the flare's SXR emission rises gradually over $\approx$ 1.5 h. Usually, the impulsive phase of flares is relatively short ($\lesssim$ 15 min: Veronig et al. 2002). If the CME follows the standard model, we would expect a more impulsive rise in SXR emission rather than a gradual one.

Secondly, according to the Coordinated Data Analysis Workshop catalog (CDAW: Yashiro et al. 2004; Gopalswamy et al. 2009), the studied CME had a kinetic energy of 4.7×10^{31} erg. This is a characteristic energy that strong X-class flares have. However, the studied CME was associated only with a B-class flare. Although there is no strict relationship between the CME and flare energies, a correlation between them nonetheless exists (Kotani et al. 2023). The low strength of the associated flare was also suspicious to us.

These factors, combined with our ability to measure CME kinematics accurately, motivated us to study the timing between the CME acceleration and flare dynamics, which we will do below.

3.2. Kinematics

To measure the CME coordinates, we need to choose a feature to track. Since in CHIP and PICS images we see only an erupting prominence, we measured the coordinates of its apex.

For measurements, we used a simple point-and-click procedure. This approach is somewhat subjective. To eliminate subjectivity and estimate errors, we repeated the procedure 9 times and averaged the result.

After this procedure, we obtained a set of CME coordinates observed by seven different instruments (or measurement modes). The instruments operated in different wavelength ranges and obtained images that looked different. As a result, in the time intervals where observations overlap, the coordinates measured by different instruments differ from each other by about 2 – 3%. Although small, this difference is significant when calculating derivatives. That is why the coordinates should be scaled in order to be consistent with each other.

For scaling, we adopted the procedure from Reva et al. (2016). We assumed that the CME expands uniformly and the heights measured from different instruments could be linearly scaled to one another. For more details on the procedure, see Section 3.4 in Reva et al. (2016).

After measuring and scaling the CME coordinates, we have 121 data points. Most of them cover the CME acceleration phase (see Figure 4). Additionally, the CHIP, Mk4, and PICS data points are shifted in time relative to each other. This yields an effective cadence of ≈ 1 min during the CME acceleration phase.

Now we need to calculate the CME velocity and acceleration. That is, we need to calculate derivatives. We are dealing with the case of numerous data points with irregular cadence, where the increments between adjacent points are comparable to the measurement errors. We think that in this case the most appropriate method for differentiation is a local least-squares approximation (see Appendix A).

We applied a local least-squares approximation to calculate the derivative of the coordinates and obtained the CME velocity. Then, using the same method, we calculated the velocity derivative and obtained the CME acceleration. The result is presented in Figure 4.

As we see, the CME has a complex acceleration structure. First, it impulsively accelerated to 440 km s^{-1} (peak acceleration 400 m s^{-2}). Then it quickly decelerated to 280 km s^{-1} (peak deceleration -200 m s^{-2}). Finally, it gradually accelerated up to 660 km s^{-1} over ≈ 2 h (peak acceleration 100 m s^{-2}).

This behavior deviates from the standard CME model. If a CME obeys the standard model, we do not expect a deceleration phase. We think this is an important issue. In the next sections, we will investigate its origin by comparing the timing of the acceleration phases and signatures of the flare reconnection.

3.3. Flare Dynamics

We cannot directly observe the reconnection inside the flare current sheet. That is why we must rely on indirect signatures of reconnection: HXR emission, the rise in SXR emission, flare ribbons' motion, etc.

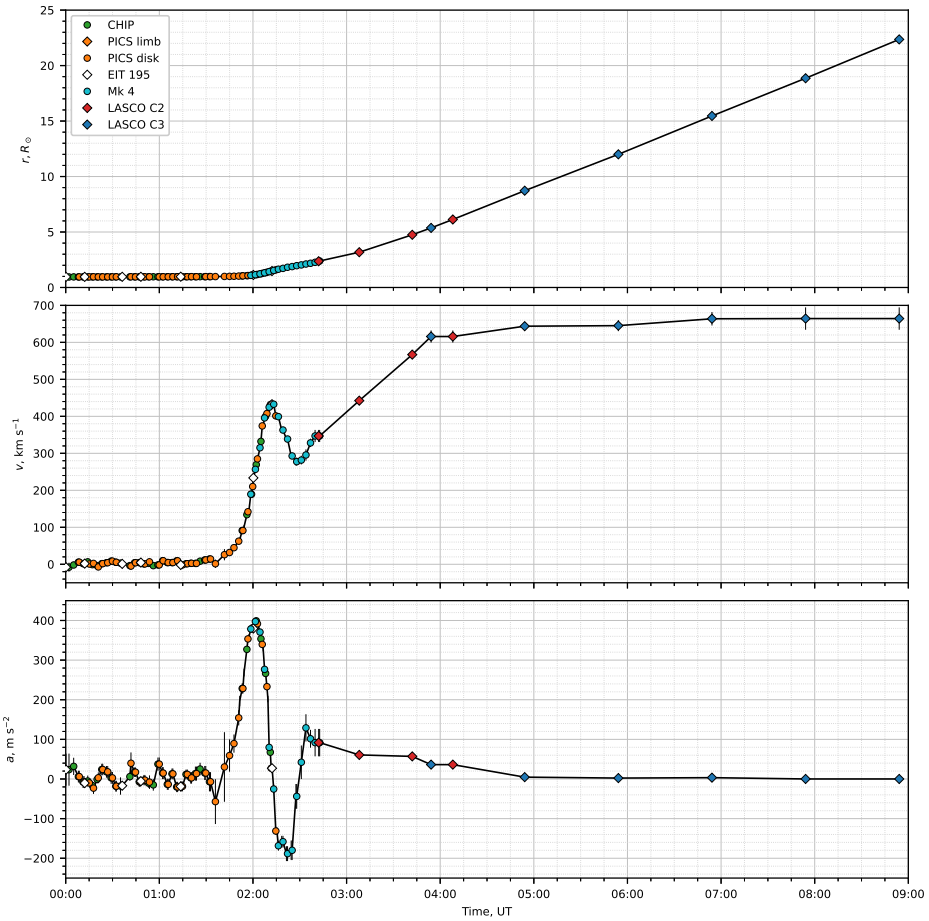


Figure 4. CME kinematics.

Usually, HXR emission is considered one of the most reliable signatures of flare reconnection. However, as stated earlier, the HXR spectrometers operating during our observations either lacked the sensitivity to detect emission from this flare or had data gaps.

An alternative signature of reconnection is the rise of the SXR emission. In the standard model, reconnection accelerates electrons. They propagate down to the chromosphere, where they stop and produce HXR emission. At the same time, accelerated electrons heat chromospheric plasma that fills the flare loops, increasing SXR emission.

So, if the flare follows the standard model, we expect reconnection to correlate with the rise of the SXR flux. Neupert (1968) formulated this more quantitatively: HXR emission correlates with the derivative of the SXR flux ("Neupert effect").

Usually, researchers use GOES 1 – 8 Å flux to analyze the Neupert effect. However, GOES provides a full-Sun integrated flux. This means that other areas of the Sun may contribute to the rise in SXR flux, which will affect the analysis.

Ideally, we need SXR images. Fortunately, we have Mg XII images available. So, to make use of the Neupert effect, we use the GOES flux and a Mg XII signal integrated over the studied active region.

Figure 3 shows GOES and Mg XII fluxes of the studied active region. We see that the SXR emission rises after the first impulsive acceleration phase of the CME. This suggests that the first acceleration phase was not related to the flare processes.

For the Neupert effect analysis, we need to calculate the derivatives. Since both GOES flux and Mg XII images have a fixed cadence, instead of a local least-squares approximation, we use the Savitzky-Golay filter (see Appendix A).

The result is presented in Figure 3. As we can see, the large values of the SXR derivative occur after the first impulsive acceleration phase of the CME.

3.4. Motion of Flare Ribbons

When accelerated electrons stop in the chromosphere, they produce bright emission at the footpoints of the flare loop. If the flaring active region has a loop arcade structure, these brightenings form two parallel ribbons (also called "flare ribbons"). As reconnection continues, larger loops become involved in the process. This will lead to flare ribbons moving away from each other. The motion of flare ribbons is directly connected to reconnection inside the current sheet, and it can serve as a proxy for flare reconnection (Qiu et al. 2004; Hinterreiter et al. 2018; Zhu et al. 2020).

For our flare, the flare ribbons are well observed in the EIT 195 Å images (see Figure 5). They are also observed in CHIP images, but they are significantly more blurred and are inconvenient for measurements. In the PICS images, flare ribbons are only seen at the late stages of the flare, and they are also harder to distinguish compared to the EIT 195 Å images. For these reasons, we use only the EIT 195 Å images for flare ribbon analysis.

First, we should note that the distance between the ribbons observed in the images is subject to projection effects. It differs from the true value by a constant scale factor. However, since we are interested only in the timing of the motion, we do not correct the obtained values for the projection effects.

Second, the "distance between the ribbons" is a vague concept. As can be seen from Figure 5, the ribbons are curved; they are not strictly parallel to each other, and the distance between them varies along the ribbons' length. So, any definition of the distance between the ribbons should be treated as a general measure of their separation.

We define the distance between the ribbons as follows. The ribbons around their center (the area around points O, A, and B in Figure 5) are approximately parallel to each other. So, we define the distance between the ribbons as the length of the line that is perpendicular (as seen in the images) to both ribbons in this area (BH in Figure 5).

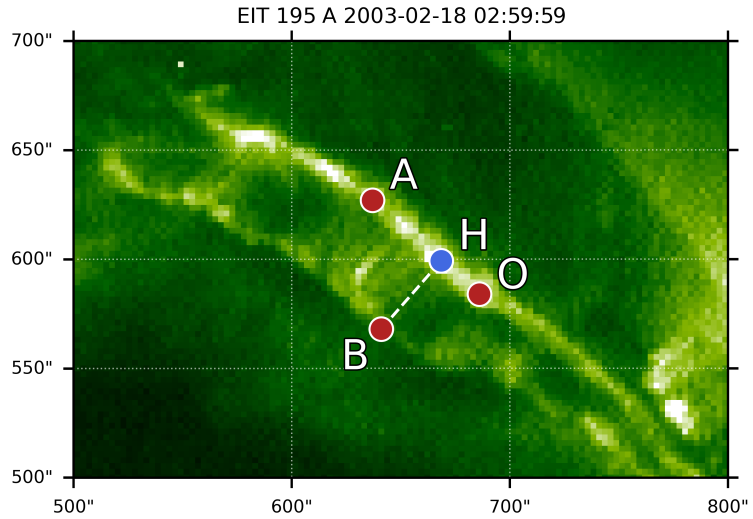


Figure 5. Measurement of the distance between the flare ribbons.

To measure this distance quantitatively, we use the following procedure. We mark three points near the center of the ribbons: two points lying on one ribbon, and the third one lying on the second ribbon (see Figure 5). Vectors $\overrightarrow{OA} = \mathbf{a} = (a_x, a_y)$ and $\overrightarrow{OB} = \mathbf{b} = (b_x, b_y)$ form a parallelogram. On the one hand, its area equals $S = |\mathbf{a} \times \mathbf{b}|$. On the other hand, $S = h|\mathbf{a}|$ (where h is the distance between the ribbons). Combining these two expressions, we obtain an expression for h:

$$h = \frac{|\mathbf{a} \times \mathbf{b}|}{|\mathbf{a}|} = \frac{|a_x b_y - a_y b_x|}{\sqrt{a_x^2 + a_y^2}} \tag{1}$$

Similar to the CME kinematics, we marked the positions of points O, A, and B using a point-and-click procedure, which is subjective. To eliminate the subjectivity, we repeated the procedure 9 times and averaged the distances. The result is presented in Figure 6.

Next, we need to calculate the derivative of h. We have a small number of data points (only 24). Therefore, a local least-squares approximation and Savitzky-Golay filters are not wise choices (see Appendix A). The displacement between adjacent data points is comparable to, or less than, the measurement error. Therefore, a finite-difference approach is also a poor choice. As we see, for the derivative of h, the forward fitting is the best choice.

For forward fitting, we need to choose a reasonable analytical expression for the speed of the ribbon separation. Unfortunately, we have no insight into how the speed should depend on time. For this reason, we pick the simplest piecewise analytical function.

The first frame in which flare ribbons were observed was at 02:12 UT. The previous frame was recorded at 02:00 UT. We assume that before $t_0 = 02{:}12$ UT, the speed of the ribbons' motion is zero. We then assume that the ribbons move

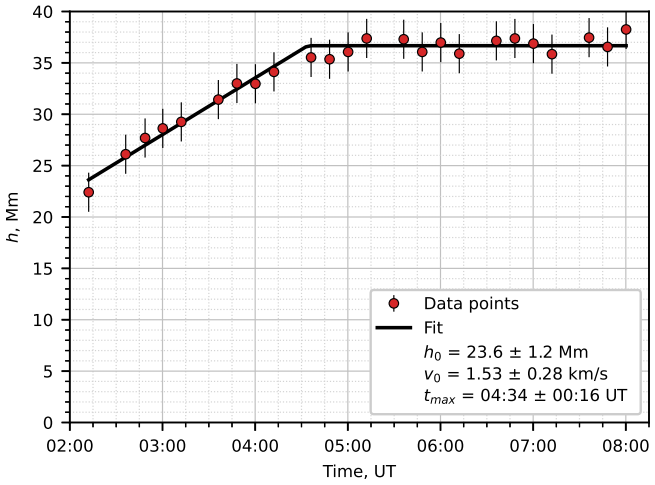


Figure 6. Time dependence of the distance between the flare ribbons.

at a constant speed v_0 until reconnection ends at $t_{\max}$. After $t_{\max}$, the speed is zero.

$$v(t) = \begin{cases} v_0, & t_0 \le t \le t_{\max} \\ 0, & \text{otherwise} \end{cases} \tag{2}$$

We integrated $v(t)$ and obtained an expression for $h(t)$:

$$h(t) = \begin{cases} h_0, & t < t_0 \\ h_0 + v_0(t - t_0), & t_0 \le t \le t_{\max} \\ h_0 + v_0(t_{\max} - t_0), & t > t_{\max} \end{cases} \tag{3}$$

Then, we fitted the experimental data points with Equation (3) using a least-squares approximation (the function `scipy.optimize.curve_fit` from the `scipy` library in Python). We obtained that $t_{\max}$ = 04:34 UT. That is, the ribbons' motion (and, therefore, reconnection) starts at 02:12 UT and ends at 04:34 UT.

We marked the time interval $[t_0, t_{\max}]$ in Figure 3. As we can see, the ribbons' motion occurs after the first impulsive acceleration phase. The motion coincides in time with the deceleration and second acceleration phases. Also, the ribbon motion continues for about 1 h after the SXR flux reached its maximum.

3.5. Previous Studies

The studied event is a beautiful example of a well-distinguished prominence eruption. This beauty attracted other researchers to study it. To provide the reader with complete information, we will briefly review the results obtained by other authors.

Bao, Zhang, and Lin (2006) studied this event with almost exactly the same set of instruments (without the CHIP and Mg XII data). The authors found that the formation of the CME leading edge and dark cavity is synchronized with the filament acceleration. They also reported Hα brightenings along the filament, which they interpreted as a signature of the filament heating.

Fan (2005); Rust and LaBonte (2005); Gibson and Fan (2008); Török, Berger, and Kliem (2010) performed MHD simulations of the flux rope eruption driven by the kink instability. The authors noted that the event's morphology – an inverse-γ shape (see Figure 8 in Török, Berger, and Kliem 2010) and rotational motion (see Figure 1 in Rust and LaBonte 2005) – is consistent with their model predictions. They concluded that this event is an example of a CME driven by the kink instability.

Finally, Maričić et al. (2007) analyzed this event in their statistical study. The authors studied the delay timing between flares and CME acceleration. To calculate acceleration, the authors used Mk4 and LASCO data. For this event, they obtained a two-stage acceleration (see Figure 6d in Maričić et al. 2007). Because the authors used less data than in this work and used spline fitting to calculate derivatives, they could not resolve a deceleration phase.

4. Discussion

4.1. Interpretation

In this work, we compared the timing of CME acceleration and flare reconnection. The comparison yielded two non-trivial results.

First, the CME showed a complex acceleration structure. It consisted of the main impulsive acceleration phase, deceleration phase, and a secondary acceleration phase. This structure is inconsistent with the standard model and deserves explanation.

Second, most of the CME acceleration occurred during the first acceleration phase, which occurred before signatures of the flare reconnection appeared (rise of the SXR and flare ribbons' motion). Again, this is inconsistent with the standard model.

Since the first acceleration phase occurred without signatures of reconnection, it is natural to explain it as a result of the ideal MHD instability: either kink (Hood and Priest 1981) or torus instability (Kliem and Török 2006). Both scenarios can explain pre-flare acceleration. However, due to its morphology (an inverse-γ shape and rotational motion), it is often used as an example of a CME driven by the kink instability (Fan 2005; Rust and LaBonte 2005; Gibson and Fan 2008; Török, Berger, and Kliem 2010). For this reason, we think that kink instability is a more likely scenario.

As for the deceleration and second acceleration phases, MHD simulations offer a hint for their explanation. Several researchers used MHD simulations to investigate whether a CME eruption is possible without flare reconnection (Fan 2005; Inoue and Kusano 2006; Török and Kliem 2007; Rachmeler, DeForest, and Kankelborg 2009). The authors showed that the CME could indeed erupt due to

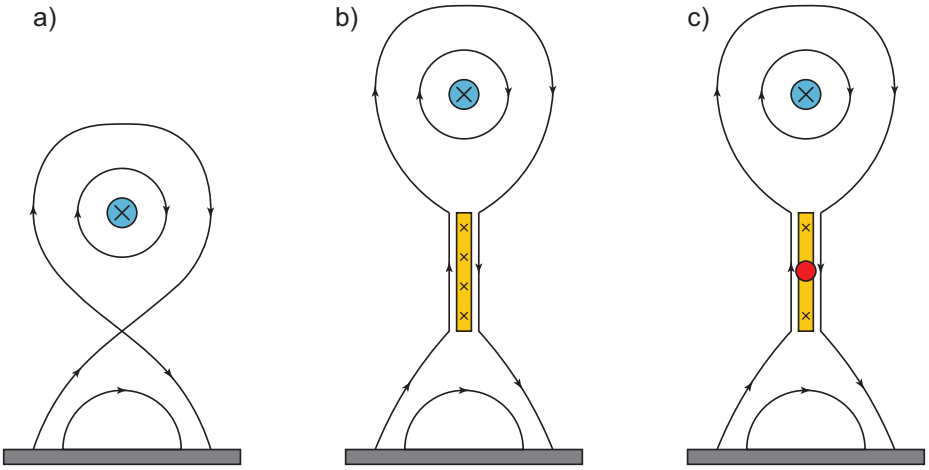


Figure 7. Interpretation of the observations. **a**) CME pre-eruption configuration. **b**) CME motion creates the current sheet. **c**) Reconnection leads to the second acceleration phase. *Blue*: current inside the flux rope; *yellow*: current inside the current sheet; *red*: reconnection.

the ideal MHD instability. Furthermore, Rachmeler, DeForest, and Kankelborg (2009) ran a simulation in the complete absence of reconnection, and the CME could still erupt. However, the motion of the flux rope creates a current sheet below it (Fan 2005; Inoue and Kusano 2006). Eventually, because of numerical resistivity, reconnection starts inside the newly formed current sheet.

The formation of the current sheet below the erupting flux rope is natural in ideal MHD. It ensures that connectivity of the magnetic field lines is preserved during flux rope motion. Therefore, it is reasonable to assume that a current sheet also formed in our case.

The current inside the current sheet will have the same direction as the current inside the flux rope (this can be derived from the direction of the magnetic field around the currents; see Figure 7). Since two currents with the same direction attract, the flux rope should experience deceleration.

The same conclusion could be made from an energy perspective. The potential magnetic field has the lowest energy. Introducing a current inside the field requires energy, which could be taken from the CME's kinetic energy.

Inoue and Kusano (2006) reproduced a similar effect. The authors ran MHD simulations of a flux rope eruption driven by the kink instability. They found that the flux rope quickly accelerates to a maximum velocity, but then its velocity drops to about half its peak value.

As the flux rope erupts, the current sheet length should increase. At some point, it should become unstable, and reconnection will start inside it. At this point, the standard model should describe the CME evolution and explain the second acceleration phase.

To summarize, we think the following model explains the observations. The CME eruption (its first impulsive acceleration phase) is caused by the kink instability. As the CME moves, a current sheet is formed below it. The interaction between the currents inside the flux rope and the current sheet slows down

the CME (the deceleration phase). Eventually, reconnection starts inside the current sheet, and the CME evolves according to the standard model (second acceleration phase).

4.2. Likelihood of the Scenario

4.2.1. General Remarks

The studied event looked like a typical CME. We observed a large erupting prominence, a three-part CME structure, rise of the SXR emission, motion of flare ribbons, and a flare arcade. These observational signatures are common for CMEs, and they fit well into the standard model. However, the CME kinematics had an anomaly. This raises a question: how common is this kinematics anomaly among other typically looking CMEs?

Clearly, we cannot answer this question based on a study of a single event. However, we will try to make an educated guess based on the reports of similar events present in the literature. Below, we will do this from several viewpoints: case studies, simulations, and statistics.

4.2.2. Case Studies

Although very rare, several studies report events that show CME-flare desynchronization and CMEs with multiple stages of impulsive acceleration.

Wang et al. (2023) reported a prominence eruption associated with a B-class flare. The CME impulsive acceleration phase occurred within the AIA field of view. This allowed them to measure its acceleration with good temporal resolution. The authors showed that the CME reached maximum velocity before the flare started. They interpreted this as evidence that the CME erupted due to the ideal MHD instability.

Song et al. (2015) reported the CME with two impulsive acceleration phases. The first phase occurred before the flare, while the second one was synchronized with the HXR emission. The authors concluded that an ideal MHD instability caused the first phase, while flare reconnection caused the second one.

Reva et al. (2017) and Byrne et al. (2014) reported CMEs with a similar acceleration pattern: impulsive acceleration, impulsive deceleration, and impulsive acceleration. However, in Reva et al. (2017), this pattern was caused by the CME-CME interaction. In Byrne et al. (2014), both acceleration phases of the studied CME were accompanied by M-class flares. The authors interpreted the acceleration phase as resulting from flare reconnection, while the deceleration phase resulted from the downward tension force of overlying field lines.

These reports show that our event is not unique. Probably, more CMEs may have similar acceleration patterns.

4.2.3. Simulations

MHD simulations reproduce the main aspects of our interpretation. Fan (2005); Inoue and Kusano (2006); Török and Kliem (2007); Rachmeler, DeForest, and

Kankelborg (2009) simulated CME eruptions caused by the ideal MHD instability. In their simulations, the current sheet forms below the flux rope, and reconnection eventually starts inside it (Fan 2005; Inoue and Kusano 2006). Furthermore, in Inoue and Kusano (2006), after acceleration caused by the kink instability, the flux rope decreases its velocity from the maximum value. As we see, from the MHD simulation viewpoint, our interpretation is plausible.

The closest to our work acceleration structure was reproduced by Guo et al. (2026). The authors performed a data-driven MHD simulation of the CME and obtained a similar pattern: impulsive acceleration, deceleration, and a second impulsive acceleration. However, they interpreted the deceleration as resulting from the downward tension force. Another difference is that, in their work, the second acceleration phase was stronger than the first.

4.2.4. Statistics

As for statistical studies, we are interested in the delay between the peaks of CME acceleration and flare reconnection. As a signature of flare reconnection, researchers use HXR emission, the derivative of SXR emission, or the reconnection rate derived from the flare ribbons' motion.

In Berkebile-Stoiser et al. (2012), for 20 out of 21 events, the peaks of CME acceleration and flare HXR emission differ by less than 10 min. In only one event in their sample, the CME acceleration peak occurred 20 min before the HXR peak.

Zhu et al. (2020) studied the relationship between CME acceleration and the reconnection rate derived from flare ribbons' motion. The authors found that the delay between the peaks of the CME acceleration and reconnection rate is less than 15 min.

For 57 events studied by Bein et al. (2012), 81% had a delay between peaks of CME acceleration and GOES SXR derivative of less than 10 min. All events except one in their sample had a delay of less than 20 min. In a similar study of 22 events by Maričić et al. (2007), the delay was less than 20 min for 75% of events, while for 25% it was higher.

Before making conclusions, we would like to comment on the limitations of these studies. Firstly, almost any method of calculating a derivative of the experimental data either explicitly or implicitly involves smoothing (see Appendix A). If smoothing is done over three neighboring data points (best-case scenario), the effective cadence is doubled. Since we need to take the derivative twice to calculate acceleration, the effective temporal resolution of the acceleration should be about three times the cadence of the original data. In the above-mentioned studies, the data cadence was $3-5$ min. Therefore, the accuracy of the acceleration timings should be about $10-15$ min.

Second, GOES registers full-Sun integrated flux. As a result, signals from two flares may overlap, which may lead to wrong CME-flare identifications (see Section 3.1 in Reva et al. 2024). In turn, this may spoil the CME-flare delay statistics. Notably, studies based on HXR emission or the reconnection rate show better synchronization than those based on GOES flux.

Considering these limitations, we think that the statistical studies show excellent CME-flare synchronization. Nonetheless, we could use the reported deviations as an upper limit on the desynchronization frequency. That is, we should expect a notable CME-flare desynchronization in less than 25% of the CMEs.

Another hint could be drawn from the statistics of CME-flare energetics. As we mentioned in the Introduction, the energetic characteristics of the CMEs and flares correlate well for strong flares and poorly for weak ones (Zhu et al. 2020; Reva et al. 2024). Probably, the CME-flare synchronization depends on the ratio of the non-potential magnetic energy that feeds the flare and the energy of the twisted magnetic field inside the flux rope. If the flare magnetic energy is significantly greater than the twisted magnetic energy, then synchronization should be good. Otherwise, we should observe a desynchronization. Therefore, it is reasonable to assume that desynchronization is more likely for CMEs associated with weak flares.

5. Conclusion

In this work, we analyzed a CME that exhibited deviation from the standard CME model. We observed the CME's evolution continuously from the solar surface to the boundary of the LASCO field of view. Good data coverage allowed a detailed comparison of CME acceleration with markers of flare reconnection.

We found that the CME had a complex acceleration structure. First, the CME impulsively accelerated, then decelerated, and then accelerated again. The markers of the reconnection – derivative of the SXR emission and motion of flare ribbons – coincided with the deceleration and second acceleration phases. In contrast, the first acceleration occurred without reconnection signatures.

We interpreted the first acceleration phase as a consequence of the kink instability. The flux rope's motion stretched the magnetic field below it, forming a current sheet. In turn, this slowed the CME. Eventually, reconnection started inside the newly formed current sheet, causing the CME to accelerate again.

These results show that CMEs can deviate from the standard model: they can significantly accelerate without magnetic reconnection and exhibit a complex acceleration structure. This means that CMEs are complex phenomena in which different mechanisms play a role in acceleration at different stages of their evolution.

Appendix

A. Calculation of the derivatives

Calculating derivatives from experimentally measured data is a complex issue. Values are measured with finite accuracy. Because differentiation involves subtracting measured values, the relative errors in the derivative increase. To address this problem, researchers have developed multiple differentiation methods (Wood 1982).

In this research, we calculate derivatives in three cases: CME speed and acceleration, SXR derivatives, and flare ribbons' motion. In each case, we use a different method. Below, we will briefly overview the methods used for calculating the derivatives, present our thoughts on their strengths and weaknesses, and explain why we choose a particular method for a particular case.

In studies of CME kinematics, the most common methods for calculating derivatives are finite difference and forward fitting approaches. In the finite difference approach, one takes two adjacent data points and divides the difference in coordinates by the time difference. This approach may give reasonable results if the coordinate difference is much larger than the measurement errors (Zhang et al. 2001, 2004; Gopalswamy et al. 2018).

However, the error of the derivative is $\sim \Delta x/\Delta t$ (where Δx is the error of the coordinate, and Δt is the instrument cadence). If we improve the cadence (i.e., make the data better), the error of the derivative will rise (i.e., make the result worse). As a result, the method gives large errors for high-cadence observations, where CME displacement for adjacent images is comparable to the instrument spatial resolution (Wang et al. 2023). In all three cases analyzed in this work, we face exactly this situation. Therefore, the finite difference approach is undesirable.

In the forward fitting approach, one assumes that the CME acceleration, velocity, or coordinates are described by an analytical formula. For example, one can assume a bell-shaped acceleration profile (Gallagher, Lawrence, and Dennis 2003; Sheeley, Warren, and Wang 2007; Reva et al. 2016; Zhu et al. 2020; Vievering et al. 2023) or a polynomial (Yashiro et al. 2004; Vršnak, Sudar, and Ruzdjak 2005; Ma et al. 2010) or spline (Vršnak et al. 2007; Maričić et al. 2007; Berkebile-Stoiser et al. 2012; Bein et al. 2012) form for coordinates. Then one calculates the analytical expression for coordinates (if needed) and fits the formula to the experimental data with a least-squares procedure. After the fitting, one analytically calculates the acceleration.

The forward fitting approach gives reasonable results when a low number of data points are available. However, it does so at the expense of information about the fine structure of its dynamics. If the CME has a complex acceleration profile (Song et al. 2015; Reva et al. 2017), this information will be lost during the forward fitting.

Additionally, this method may lead to unphysical results if the analytical function is too complex. For example, if one fits the CME coordinates with a polynomial of a high degree, it could result in unphysically large accelerations at large distances.

In our research, we have a low number of coordinates measured for flare ribbons' motion, and forward fitting is a good approach in this case. In contrast, SXR light curves and CME kinematics have many data points. Applying forward fitting will lose information about the fine structure of the process. Therefore, we need another method.

When dealing with a high-cadence time series, there is a need to smooth the data. In signal processing, the standard solution is to use a Savitzky-Golay filter (Savitzky and Golay 1964; Steinier, Termonia, and Deltour 1972). In this

approach, for each data point, we approximate the data around it (within a fixed-size running window) with a low-order polynomial. Then, to smooth the data, we use the fitted value as the smoothed data point. If one needs to calculate a derivative, then the polynomial is differentiated, and the value of the derivative is obtained.

If the data points have a fixed cadence, the fitting can be expressed as a linear combination of the data points within the running window, and the coefficients of the linear combination can be calculated beforehand. That is, the whole procedure can be done as a convolution, which is computationally efficient.

In our work, the calculation of the SXR derivatives is a case of a large number of data points with a fixed cadence. This is a classic example where the Savitzky-Golay filter performs well. For this purpose, we use the `savgol_filter` function from the Python `scipy` library.

However, the CME kinematics have an irregular cadence. As a result, the Savitzky-Golay filter is not applicable, and we need something different.

A generalization of the Savitzky-Golay filter is the local least-squares approximation (Wood 1982; Reva et al. 2017, 2022). In this approach, similar to the Savitzky-Golay filter, we approximate the data within a running window with a linear function. The slope of the fit is the derivative. However, because the data points are irregularly spaced and the number of points in the window varies, we cannot express the operation as a convolution and need to make a fit for each point. This is more computationally expensive than the Savitzky-Golay filter, but it is a more general approach. We think this approach is best for calculating the derivatives of the CME kinematics.

Acknowledgements For data analysis and visualization, we used the following Python packages: `matplotlib` (Hunter 2007), `numpy` (Harris et al. 2020), `scipy` (Virtanen et al. 2020), `pandas` (Wes McKinney 2010), and `sunpy` (SunPy Community et al. 2020). Mk4 coronameter (https://doi.org/10.5065/d66972c9), PICS (https://doi.org/10.5065/d65719tr), and CHIP (https://doi.org/10.5065/d6ww7gf7) data are provided courtesy of the Mauna Loa Solar Observatory, operated by the High Altitude Observatory, as part of the National Center for Atmospheric Research (NCAR). NCAR is supported by the National Science Foundation. SXI full-disk X-ray images are supplied courtesy of the Solar X-ray Imager (SXI) team. The SOHO/LASCO data are produced by a consortium of the Naval Research Laboratory (USA), Max-Planck-Institut fur Aeronomie (Germany), Laboratoire d'Astronomie (France), and the University of Birmingham (UK). EIT data are supplied courtesy of the SOHO/MDI and SOHO/EIT consortia. SOHO is a project of international cooperation between ESA and NASA.

Author Contribution A.A. Reva and A.S. Kirichenko measured the CME kinematics and flare ribbons' motion. A.A. Reva and I.P. Loboda prepared illustrations. A.A. Reva, I.P. Loboda, and A.S. Bogachev wrote the text of the manuscript. All authors read and approved the final manuscript.

Funding This research was funded by a grant from the Russian Science Foundation (grant No 23-72-30002, https://rscf.ru/project/23-72-30002/).

Data Availability Mk4, PICS, and CHIP data are openly available at https://mlso.hao.ucar.edu/mlso_data_calendar.php. SXI data are openly available at https://www.ncei.noaa.gov/data/goes-solar-xray-imager/. LASCO and EIT data are openly available at https://sdac.virtualsolar.org/cgi/search. The Mg XII spectroheliograph data are available from the corresponding author on reasonable request.

Declarations

Conflict of interest The authors declare that they have no conflicts of interest.

References

Alissandrakis, C.E., Kochanov, A.A., Patsourakos, S., Altyntsev, A.T., Lesovoi, S.V., Lesovoya, N.N.: 2013, Microwave and EUV Observations of an Erupting Filament and Associated Flare and Coronal Mass Ejections. *Publ. Astron. Soc. Japan* **65**, 8. DOI. ADS.

Andrews, M.D.: 2003, A Search for CMEs Associated with Big Flares. *Sol. Phys.* **218**, 261. DOI. ADS.

Aptekar, R.L., Frederiks, D.D., Golenetskii, S.V., Ilynskii, V.N., Mazets, E.P., Panov, V.N., Sokolova, Z.J., Terekhov, M.M., Sheshin, L.O., Cline, T.L., Stilwell, D.E.: 1995, Konus-W Gamma-Ray Burst Experiment for the GGS Wind Spacecraft. *Space Sci. Rev.* **71**, 265. DOI. ADS.

Bao, X.-M., Zhang, H.-Q., Lin, J.: 2006, Formation of the CME Leading Edge Observed in the 2003 February 18 Event. *Chin. J. Astron. Astrophys.* **6**, 741. ADS.

Bein, B.M., Berkebile-Stoiser, S., Veronig, A.M., Temmer, M., Vršnak, B.: 2012, Impulsive Acceleration of Coronal Mass Ejections. II. Relation to Soft X-Ray Flares and Filament Eruptions. *Astrophys. J.* **755**, 44. DOI. ADS.

Bemporad, A., Raymond, J., Poletto, G., Romoli, M.: 2007, A Comprehensive Study of the Initiation and Early Evolution of a Coronal Mass Ejection from Ultraviolet and White-Light Data. *Astrophys. J.* **655**, 576. DOI. ADS.

Berkebile-Stoiser, S., Veronig, A.M., Bein, B.M., Temmer, M.: 2012, Relation between the Coronal Mass Ejection Acceleration and the Non-thermal Flare Characteristics. *Astrophys. J.* **753**, 88. DOI. ADS.

Brueckner, G.E., Howard, R.A., Koomen, M.J., Korendyke, C.M., Michels, D.J., Moses, J.D., Socker, D.G., Dere, K.P., Lamy, P.L., Llebaria, A., Bout, M.V., Schwenn, R., Simnett, G.M., Bedford, D.K., Eyles, C.J.: 1995, The Large Angle Spectroscopic Coronagraph (LASCO). *Sol. Phys.* **162**, 357. DOI. ADS.

Byrne, J.P., Morgan, H., Seaton, D.B., Bain, H.M., Habbal, S.R.: 2014, Bridging EUV and White-Light Observations to Inspect the Initiation Phase of a "Two-Stage" Solar Eruptive Event. *Sol. Phys.* **289**, 4545. DOI. ADS.

Carmichael, H.: 1964, A Process for Flares. *NASA Special Publication* **50**, 451. ADS.

Chen, P.F.: 2011, Coronal Mass Ejections: Models and Their Observational Basis. *Living Reviews in Solar Physics* **8**. DOI. http://www.livingreviews.org/lrsp-2011-1.

Delaboudinière, J., Artzner, G.E., Brunaud, J., Gabriel, A.H., Hochedez, J.F., Millier, F., Song, X.Y., Au, B., Dere, K.P., Howard, R.A., Kreplin, R., Michels, D.J., Moses, J.D., Defise, J.M., Jamar, C., Rochus, P., Chauvineau, J.P., Marioge, J.P., Catura, R.C., Lemen, J.R., Shing, L., Stern, R.A., Gurman, J.B., Neupert, W.M., Maucherat, A., Clette, F., Cugnon, P., van Dessel, E.L.: 1995, EIT: Extreme-Ultraviolet Imaging Telescope for the SOHO Mission. *Sol. Phys.* **162**, 291. DOI. ADS.

D'Huys, E., Seaton, D.B., De Groof, A., Berghmans, D., Poedts, S.: 2017, Solar signatures and eruption mechanism of the August 14, 2010 coronal mass ejection (CME). *Journal of Space Weather and Space Climate* **7**, A7. DOI. ADS.

Dmitriev, P.B., Kudryavtsev, I.V., Lazutkov, V.P., Matveev, G.A., Savchenko, M.I., Skorodumov, D.V., Charikov, Y.E.: 2006, Solar flares registered by the IRIS spectrometer onboard the CORONAS-F satellite: Peculiarities of the X-ray emission. *Solar System Research* **40**, 142. DOI. ADS.

Domingo, V., Fleck, B., Poland, A.I.: 1995, The SOHO Mission: an Overview. *Sol. Phys.* **162**, 1. DOI. ADS.

Elmore, D.F., Burkepile, J.T., Darnell, J.A., Lecinski, A.R., Stanger, A.L.: 2003, Calibration of a ground-based solar coronal polarimeter. In: Fineschi, S. (ed.) *Polarimetry in Astronomy*, *Society of Photo-Optical Instrumentation Engineers (SPIE) Conference Series* **4843**, 66. DOI. ADS.

Fan, Y.: 2005, Coronal Mass Ejections as Loss of Confinement of Kinked Magnetic Flux Ropes. *Astrophys. J.* **630**, 543. DOI. ADS.

Frederiks, D.D., Golenetskii, S.V., Palshin, V.D., Aptekar, R.L., Ilyinskii, V.N., Oleinik, F.P., Mazets, E.P., Cline, T.L.: 2007, Giant flare in SGR 1806-20 and its Compton reflection from the Moon. *Astronomy Letters* **33**, 1. DOI. ADS.

Gallagher, P.T., Lawrence, G.R., Dennis, B.R.: 2003, Rapid Acceleration of a Coronal Mass Ejection in the Low Corona and Implications for Propagation. *Astrophys. J. Lett.* **588**, L53. DOI. ADS.

Gibson, S.E., Fan, Y.: 2008, Partially ejected flux ropes: Implications for interplanetary coronal mass ejections. *Journal of Geophysical Research (Space Physics)* **113**, A09103. DOI. ADS.

Gopalswamy, N., Yashiro, S., Michalek, G., Stenborg, G., Vourlidas, A., Freeland, S., Howard, R.: 2009, The SOHO/LASCO CME Catalog. *Earth Moon and Planets* **104**, 295. DOI. ADS.

Gopalswamy, N., Yashiro, S., Mäkelä, P., Xie, H., Akiyama, S., Monstein, C.: 2018, Extreme Kinematics of the 2017 September 10 Solar Eruption and the Spectral Characteristics of the Associated Energetic Particles. *Astrophys. J. Lett.* **863**, L39. DOI. ADS.

Guo, J.H., Poedts, S., Schmieder, B., Guo, Y., Zhou, C., Wu, H., Ni, Y.W., Zhong, Z., Zhou, Y.H., Li, S.H., Chen, P.F.: 2026, Data-driven magnetohydrodynamic simulation of the initiation of a coronal mass ejection with multiple stages. *Astron. Astrophys.* **707**, L5. DOI. ADS.

Hanser, F.A., Sellers, F.B.: 1996, Design and calibration of the GOES-8 solar x-ray sensor: the XRS. In: Washwell, E.R. (ed.) *GOES-8 and Beyond*, *Society of Photo-Optical Instrumentation Engineers (SPIE) Conference Series* **2812**, 344. DOI. ADS.

Harris, C.R., Millman, K.J., van der Walt, S.J., Gommers, R., Virtanen, P., Cournapeau, D., Wieser, E., Taylor, J., Berg, S., Smith, N.J., Kern, R., Picus, M., Hoyer, S., van Kerkwijk, M.H., Brett, M., Haldane, A., del Río, J.F., Wiebe, M., Peterson, P., Gérard-Marchant, P., Sheppard, K., Reddy, T., Weckesser, W., Abbasi, H., Gohlke, C., Oliphant, T.E.: 2020, Array programming with NumPy. *Nature* **585**, 357. DOI. ADS.

Hill, S.M., Pizzo, V.J., Balch, C.C., Biesecker, D.A., Bornmann, P., Hildner, E., Lewis, L.D., Grubb, R.N., Husler, M.P., Prendergast, K., Vickroy, J., Greer, S., Defoor, T., Wilkinson, D.C., Hooker, R., Mulligan, P., Chipman, E., Bysal, H., Douglas, J.P., Reynolds, R., Davis, J.M., Wallace, K.S., Russell, K., Freestone, K., Bagdigian, D., Page, T., Kerns, S., Hoffman, R., Cauffman, S.A., Davis, M.A., Studer, R., Berthiaume, F.E., Saha, T.T., Berthiume, G.D., Farthing, H., Zimmermann, F.: 2005, The NOAA Goes-12 Solar X-Ray Imager (SXI) 1. Instrument, Operations, and Data. *Sol. Phys.* **226**, 255. DOI. ADS.

Hinterreiter, J., Veronig, A.M., Thalmann, J.K., Tschernitz, J., Pötzi, W.: 2018, Statistical Properties of Ribbon Evolution and Reconnection Electric Fields in Eruptive and Confined Flares. *Sol. Phys.* **293**, 38. DOI. ADS.

Hirayama, T.: 1974, Theoretical Model of Flares and Prominences. I: Evaporating Flare Model. *Sol. Phys.* **34**, 323. DOI. ADS.

Hood, A.W., Priest, E.R.: 1981, Critical conditions for magnetic instabilities in force-free coronal loops. *Geophysical and Astrophysical Fluid Dynamics* **17**, 297. DOI. ADS.

Hunter, J.D.: 2007, Matplotlib: A 2D Graphics Environment. *Computing in Science and Engineering* **9**, 90. DOI. ADS.

Illing, R.M.E., Hundhausen, A.J.: 1985, Observation of a coronal transient from 1.2 to 6 solar radii. *J. Geophys. Res.* **90**, 275. DOI. ADS.

Inoue, S., Kusano, K.: 2006, Three-dimensional Simulation Study of Flux Rope Dynamics in the Solar Corona. *Astrophys. J.* **645**, 742. DOI. ADS.

Jing, J., Qiu, J., Lin, J., Qu, M., Xu, Y., Wang, H.: 2005, Magnetic Reconnection Rate and Flux-Rope Acceleration of Two-Ribbon Flares. *Astrophys. J.* **620**, 1085. DOI. ADS.

Kirichenko, A.S., Bogachev, S.A.: 2017, Plasma Heating in Solar Microflares: Statistics and Analysis. *Astrophys. J.* **840**, 45. DOI. ADS.

Kirichenko, A.S., Reva, A.A., Bogachev, S.A., Loboda, I.P.: 2024, Changes in the Structure of the Sun's Activity Belts from Flares to Nanoflares. *Astrophysical Bulletin* **79**, 674. DOI. ADS.

Kliem, B., Török, T.: 2006, Torus Instability. *Physical Review Letters* **96**, 255002. DOI. ADS.

Kopp, R.A., Pneuman, G.W.: 1976, Magnetic reconnection in the corona and the loop prominence phenomenon. *Sol. Phys.* **50**, 85. DOI. ADS.

Kotani, Y., Shibata, K., Ishii, T.T., Yamasaki, D., Otsuji, K., Ichimoto, K., Asai, A.: 2023, Unified Relationship between Cold Plasma Ejections and Flare Energies Ranging from Solar Microflares to Giant Stellar Flares. *Astrophys. J.* **943**, 143. DOI. ADS.

Lemen, J.R., Title, A.M., Akin, D.J., Boerner, P.F., Chou, C., Drake, J.F., Duncan, D.W., Edwards, C.G., Friedlaender, F.M., Heyman, G.F., Hurlburt, N.E., Katz, N.L., Kushner, G.D., Levay, M., Lindgren, R.W., Mathur, D.P., McFeaters, E.L., Mitchell, S., Rehse, R.A., Schrijver, C.J., Springer, L.A., Stern, R.A., Tarbell, T.D., Wuelser, J.-P., Wolfson, C.J., Yanari, C., Bookbinder, J.A., Cheimets, P.N., Caldwell, D., Deluca, E.E., Gates, R., Golub, L., Park, S., Podgorski, W.A., Bush, R.I., Scherrer, P.H., Gummin, M.A., Smith, P., Auker, G., Jerram, P., Pool, P., Soufli, R., Windt, D.L., Beardsley, S., Clapp, M., Lang, J., Waltham, N.: 2012, The Atmospheric Imaging Assembly (AIA) on the Solar Dynamics Observatory (SDO). *Sol. Phys.* **275**, 17. DOI. ADS.

Lin, R.P., Dennis, B.R., Hurford, G.J., Smith, D.M., Zehnder, A., Harvey, P.R., Curtis, D.W., Pankow, D., Turin, P., Bester, M., Csillaghy, A., Lewis, M., Madden, N., van Beek, H.F., Appleby, M., Raudorf, T., McTiernan, J., Ramaty, R., Schmahl, E., Schwartz, R., Krucker, S., Abiad, R., Quinn, T., Berg, P., Hashii, M., Sterling, R., Jackson, R., Pratt, R., Campbell, R.D., Malone, D., Landis, D., Barrington-Leigh, C.P., Slassi-Sennou, S., Cork, C., Clark, D., Amato, D., Orwig, L., Boyle, R., Banks, I.S., Shirey, K., Tolbert, A.K., Zarro, D., Snow, F., Thomsen, K., Henneck, R., McHedlishvili, A., Ming, P., Fivian, M., Jordan, J., Wanner, R., Crubb, J., Preble, J., Matranga, M., Benz, A., Hudson, H., Canfield, R.C., Holman, G.D., Crannell, C., Kosugi, T., Emslie, A.G., Vilmer, N., Brown, J.C., Johns-Krull, C., Aschwanden, M., Metcalf, T., Conway, A.: 2002, The Reuven Ramaty High-Energy Solar Spectroscopic Imager (RHESSI). *Sol. Phys.* **210**, 3. DOI. ADS.

Ma, S., Attrill, G.D.R., Golub, L., Lin, J.: 2010, Statistical Study of Coronal Mass Ejections With and Without Distinct Low Coronal Signatures. *Astrophys. J.* **722**, 289. DOI. ADS.

Maričić, D., Vršnak, B., Stanger, A.L., Veronig, A.M., Temmer, M., Roša, D.: 2007, Acceleration Phase of Coronal Mass Ejections: II. Synchronization of the Energy Release in the Associated Flare. *Sol. Phys.* **241**, 99. DOI. ADS.

Mierla, M., Seaton, D.B., Berghmans, D., Chifu, I., De Groof, A., Inhester, B., Rodriguez, L., Stenborg, G., Zhukov, A.N.: 2013, Study of a Prominence Eruption using PROBA2/SWAP and STEREO/EUVI Data. *Sol. Phys.* **286**, 241. DOI. ADS.

Mierla, M., Zhukov, A.N., Berghmans, D., Parenti, S., Auchère, F., Heinzel, P., Seaton, D.B., Palmerio, E., Jejčič, S., Janssens, J., Kraaikamp, E., Nicula, B., Long, D.M., Hayes, L.A., Jebaraj, I.C., Talpeanu, D.-C., D'Huys, E., Dolla, L., Gissot, S., Magdalenić, J., Rodriguez, L., Shestov, S., Stegen, K., Verbeeck, C., Sasso, C., Romoli, M., Andretta, V.: 2022, Prominence eruption observed in He II 304 Å up to >6 $R_{\odot}$ by EUI/FSI aboard Solar Orbiter. *Astron. Astrophys.* **662**, L5. DOI. ADS.

Müller, D., St. Cyr, O.C., Zouganelis, I., Gilbert, H.R., Marsden, R., Nieves-Chinchilla, T., Antonucci, E., Auchère, F., Berghmans, D., Horbury, T.S., Howard, R.A., Krucker, S., Maksimovic, M., Owen, C.J., Rochus, P., Rodriguez-Pacheco, J., Romoli, M., Solanki, S.K., Bruno, R., Carlsson, M., Fludra, A., Harra, L., Hassler, D.M., Livi, S., Louarn, P., Peter, H., Schühle, U., Teriaca, L., del Toro Iniesta, J.C., Wimmer-Schweingruber, R.F., Marsch, E., Velli, M., De Groof, A., Walsh, A., Williams, D.: 2020, The Solar Orbiter mission. Science overview. *Astron. Astrophys.* **642**, A1. DOI. ADS.

Neupert, W.M.: 1968, Comparison of Solar X-Ray Line Emission with Microwave Emission during Flares. *Astrophys. J. Lett.* **153**, L59. DOI. ADS.

Oraevsky, V.N., Sobelman, I.I.: 2002, Comprehensive Studies of Solar Activity on the CORONAS-F Satellite. *Astron. Lett.* **28**, 401. DOI. ADS.

Paterson, S., Hannah, I.G., Grefenstette, B.W., Hudson, H.S., Krucker, S., Glesener, L., White, S.M., Smith, D.M.: 2023, The First Survey of Quiet Sun Features Observed in Hard X-Rays with NuSTAR. *Sol. Phys.* **298**, 47. DOI. ADS.

Pesnell, W.D., Thompson, B.J., Chamberlin, P.C.: 2012, The Solar Dynamics Observatory (SDO). *Sol. Phys.* **275**, 3. DOI. ADS.

Pizzo, V.J., Hill, S.M., Balch, C.C., Biesecker, D.A., Bornmann, P., Hildner, E., Grubb, R.N., Chipman, E.G., Davis, J.M., Wallace, K.S., Russell, K., Cauffman, S.A., Saha, T.T., Berthiume, G.D.: 2005, The NOAA Goes-12 Solar X-Ray Imager (SXI) 2. Performance. *Sol. Phys.* **226**, 283. DOI. ADS.

Prestage, N.P., Luckhurst, R.G., Paterson, B.R., Bevins, C.S., Yuile, C.G.: 1994, A New Radio Spectrograph at Culgoora. *Sol. Phys.* **150**, 393. DOI. ADS.

Pulkkinen, T.: 2007, Space Weather: Terrestrial Perspective. *Living Reviews in Solar Physics* **4**. DOI. http://www.livingreviews.org/lrsp-2007-1.
Qiu, J., Wang, H., Cheng, C.Z., Gary, D.E.: 2004, Magnetic Reconnection and Mass Acceleration in Flare-Coronal Mass Ejection Events. *Astrophys. J.* **604**, 900. DOI. ADS.
Rachmeler, L.A., DeForest, C.E., Kankelborg, C.C.: 2009, Reconnectionless CME Eruption: Putting the Aly-Sturrock Conjecture to Rest. *Astrophys. J.* **693**, 1431. DOI. ADS.
Reva, A.A., Ulyanov, A.S., Kuzin, S.V.: 2016, Current Sheet Structures Observed by the TESIS EUV Telescope during a Flux Rope Eruption on the Sun. *Astrophys. J.* **832**, 16. DOI. ADS.
Reva, A.A., Ulyanov, A.S., Bogachev, S.A., Kuzin, S.V.: 2014, Initiation and Early Evolution of the Coronal Mass Ejection on 2009 May 13 from Extreme-ultraviolet and White-light Observations. *Astrophys. J.* **793**, 140. DOI. ADS.
Reva, A.A., Ulyanov, A.S., Shestov, S.V., Kuzin, S.V.: 2016, Breakout Reconnection Observed by the TESIS EUV Telescope. *Astrophys. J.* **816**, 90. DOI. ADS.
Reva, A.A., Kirichenko, A.S., Ulyanov, A.S., Kuzin, S.V.: 2017, Observations of the Coronal Mass Ejection with a Complex Acceleration Profile. *Astrophys. J.* **851**, 108. DOI. ADS.
Reva, A., Ulyanov, A., Kirichenko, A., Bogachev, S., Kuzin, S.: 2018, Estimate of the Upper Limit on Hot Plasma Differential Emission Measure (DEM) in Non-Flaring Active Regions and Nanoflare Frequency Based on the Mg xii Spectroheliograph Data from CORONAS-F/SPIRIT. *Sol. Phys.* **293**, 140. DOI. ADS.
Reva, A.A., Kuzin, S.V., Kirichenko, A.S., Ulyanov, A.S., Loboda, I.P., Bogachev, S.A.: 2021, Monochromatic X-Ray Imagers of the Sun Based on the Bragg Crystal Optics. *Frontiers in Astronomy and Space Sciences* **8**, 40. DOI. https://www.frontiersin.org/article/10.3389/fspas.2021.645062.
Reva, A.A., Bogachev, S.A., Loboda, I.P., Ulyanov, A.S., Kirichenko, A.S.: 2022, Observations of Current Sheet Heating in X-Ray during a Solar Flare. *Astrophys. J.* **931**, 93. DOI. ADS.
Reva, A., Bogachev, S., Loboda, I., Kirichenko, A., Ulyanov, A.: 2023, Plasma Heating During Coronal Mass Ejections Observed in X-Rays. *Sol. Phys.* **298**, 61. DOI. ADS.
Reva, A., Loboda, I., Bogachev, S., Kirichenko, A.: 2024, CME-Flare Association and the Role of Reconnection in CME Acceleration. *Sol. Phys.* **299**, 55. DOI. ADS.
Rust, D.M., LaBonte, B.J.: 2005, Observational Evidence of the Kink Instability in Solar Filament Eruptions and Sigmoids. *Astrophys. J. Lett.* **622**, L69. DOI. ADS.
Savitzky, A., Golay, M.J.E.: 1964, Smoothing and differentiation of data by simplified least squares procedures. *Analytical Chemistry* **36**, 1627. DOI. ADS.
Schwenn, R.: 2006, Space Weather: The Solar Perspective. *Living Reviews in Solar Physics* **3**. DOI. http://www.livingreviews.org/lrsp-2006-2.
Seaton, D.B., Darnel, J.M.: 2018, Observations of an Eruptive Solar Flare in the Extended EUV Solar Corona. *Astrophys. J. Lett.* **852**, L9. DOI. ADS.
Sheeley, N.R. Jr., Warren, H.P., Wang, Y.-M.: 2007, A Streamer Ejection with Reconnection Close to the Sun. *Astrophys. J.* **671**, 926. DOI. ADS.
Slemzin, V., Bougaenko, O., Ignatiev, A., Kuzin, S., Mitrofanov, A., Pertsov, A., Zhitnik, I.: 2008, Off-limb EUV observations of the solar corona and transients with the CORONAS-F/SPIRIT telescope-coronagraph. *Annales Geophysicae* **26**, 3007. DOI. ADS.
Song, H.Q., Chen, Y., Zhang, J., Cheng, X., Fu, H., LI, G.: 2015, Acceleration Phases of a Solar Filament During Its Eruption. *Astrophys. J. Lett.* **804**, L38. DOI. ADS.
Song, H., Li, L., Zhou, Z., Xia, L., Cheng, X., Chen, Y.: 2023, The Structure of Coronal Mass Ejections Recorded by the K-Coronagraph at Mauna Loa Solar Observatory. *Astrophys. J. Lett.* **952**, L22. DOI. ADS.
Steinier, J., Termonia, Y., Deltour, J.: 1972, Smoothing and differentiation of data by simplified least square procedure. *Analytical Chemistry* **44**, 1906. DOI. ADS.
Sturrock, P.A.: 1966, Model of the High-Energy Phase of Solar Flares. *Nature* **211**, 695. DOI. ADS.
SunPy Community, Barnes, W.T., Bobra, M.G., Christe, S.D., Freij, N., Hayes, L.A., Ireland, J., Mumford, S., Perez-Suarez, D., Ryan, D.F., Shih, A.Y., Chanda, P., Glogowski, K., Hewett, R., Hughitt, V.K., Hill, A., Hiware, K., Inglis, A., Kirk, M.S.F., Konge, S., Mason, J.P., Maloney, S.A., Murray, S.A., Panda, A., Park, J., Pereira, T.M.D., Reardon, K., Savage, S., Sipőcz, B.M., Stansby, D., Jain, Y., Taylor, G., Yadav, T., Rajul, Dang, T.K.: 2020, The SunPy Project: Open Source Development and Status of the Version 1.0 Core Package. *Astrophys. J.* **890**, 68. DOI. ADS.
Svestka, Z., Cliver, E.W.: 1992, History and Basic Characteristics of Eruptive Flares. In: Svestka, Z., Jackson, B.V., Machado, M.E. (eds.) *IAU Colloq. 133: Eruptive Solar Flares* **399**, 1. DOI. ADS.

Tadikonda, S.K., Freesland, D.C., Minor, R.R., Seaton, D.B., Comeyne, G.J., Krimchansky, A.: 2019, Coronal Imaging with the Solar UltraViolet Imager. *Sol. Phys.* **294**, 28. DOI. ADS.

Temmer, M., Veronig, A.M., Vršnak, B., Rybák, J., Gömöry, P., Stoiser, S., Maričić, D.: 2008, Acceleration in Fast Halo CMEs and Synchronized Flare HXR Bursts. *Astrophys. J. Lett.* **673**, L95. DOI. ADS.

Temmer, M., Veronig, A.M., Kontar, E.P., Krucker, S., Vršnak, B.: 2010, Combined STEREO/RHESSI Study of Coronal Mass Ejection Acceleration and Particle Acceleration in Solar Flares. *Astrophys. J.* **712**, 1410. DOI. ADS.

Török, T., Kliem, B.: 2007, Numerical simulations of fast and slow coronal mass ejections. *Astronomische Nachrichten* **328**, 743. DOI. ADS.

Török, T., Berger, M.A., Kliem, B.: 2010, The writhe of helical structures in the solar corona. *Astron. Astrophys.* **516**, A49. DOI. ADS.

Ulyanov, A., Reva, A., Kirichenko, A., Loboda, I., Bogachev, S.: 2024, Solar extreme ultraviolet variability as a proxy for nanoflare heating diagnostics. *Astron. Astrophys.* **683**, A88. DOI. ADS.

Urnov, A.M., Shestov, S.V., Bogachev, S.A., Goryaev, F.F., Zhitnik, I.A., Kuzin, S.V.: 2007, On the spatial and temporal characteristics and formation mechanisms of soft X-ray emission in the solar corona. *Astronomy Letters* **33**, 396. DOI. ADS.

Veronig, A., Vršnak, B., Temmer, M., Hanslmeier, A.: 2002, Relative timing of solar flares observed at different wavelengths. *Sol. Phys.* **208**, 297. DOI. ADS.

Vievering, J.T., Vourlidas, A., Zhu, C., Qiu, J., Glesener, L.: 2023, Evolution of Solar Eruptive Events: Investigating the Relationships among Magnetic Reconnection, Flare Energy Release, and Coronal Mass Ejections. *Astrophys. J.* **946**, 81. DOI. ADS.

Virtanen, P., Gommers, R., Oliphant, T.E., Haberland, M., Reddy, T., Cournapeau, D., Burovski, E., Peterson, P., Weckesser, W., Bright, J., van der Walt, S.J., Brett, M., Wilson, J., Millman, K.J., Mayorov, N., Nelson, A.R.J., Jones, E., Kern, R., Larson, E., Carey, C.J., Polat, İ., Feng, Y., Moore, E.W., VanderPlas, J., Laxalde, D., Perktold, J., Cimrman, R., Henriksen, I., Quintero, E.A., Harris, C.R., Archibald, A.M., Ribeiro, A.H., Pedregosa, F., van Mulbregt, P., SciPy 1.0 Contributors: 2020, SciPy 1.0: Fundamental Algorithms for Scientific Computing in Python. *Nature Methods* **17**, 261. DOI. ADS.

Vršnak, B., Sudar, D., Ruzdjak, D.: 2005, The CME-flare relationship: Are there really two types of CMEs? *Astron. Astrophys.* **435**, 1149. DOI. https://doi.org/10.1051/0004-6361:20042166.

Vršnak, B., Maričić, D., Stanger, A.L., Veronig, A.M., Temmer, M., Roša, D.: 2007, Acceleration Phase of Coronal Mass Ejections: I. Temporal and Spatial Scales. *Sol. Phys.* **241**, 85. DOI. ADS.

Wang, X., Song, H., Chen, Y., Li, L., Hou, Z., Zheng, R.: 2023, The Impulsive Acceleration of a Solar Filament Eruption Associated with a B-class Flare. *Astrophys. J.* **957**, 58. DOI. ADS.

Webb, D.F., Howard, T.A.: 2012, Coronal Mass Ejections: Observations. *Living Reviews in Solar Physics* **9**. DOI. http://www.livingreviews.org/lrsp-2012-3.

Webb, D.F., Hundhausen, A.J.: 1987, Activity Associated with the Solar Origin of Coronal Mass Ejections. *Sol. Phys.* **108**, 383. DOI. ADS.

Wes McKinney: 2010, Data Structures for Statistical Computing in Python. In: Stéfan van der Walt, Jarrod Millman (eds.) *Proceedings of the 9th Python in Science Conference*, 56 . DOI.

West, M.J., Seaton, D.B., Wexler, D.B., Raymond, J.C., Del Zanna, G., Rivera, Y.J., Kobelski, A.R., Chen, B., DeForest, C., Golub, L., Caspi, A., Gilly, C.R., Kooi, J.E., Meyer, K.A., Alterman, B.L., Alzate, N., Andretta, V., Auchère, F., Banerjee, D., Berghmans, D., Chamberlin, P., Chitta, L.P., Downs, C., Giordano, S., Harra, L., Higginson, A., Howard, R.A., Kumar, P., Mason, E., Mason, J.P., Morton, R.J., Nykyri, K., Patel, R., Rachmeler, L., Reardon, K.P., Reeves, K.K., Savage, S., Thompson, B.J., Van Kooten, S.J., Viall, N.M., Vourlidas, A., Zhukov, A.N.: 2023, Defining the Middle Corona. *Sol. Phys.* **298**, 78. DOI. ADS.

Wood, G.A.: 1982, Data Smoothing and Differential Procedures in Biomechanics. *Exercise and Sport Sciences Reviews* **10**, 308. http://journals.lww.com/acsm-essr/Abstract/1982/01000/DATA_SMOOTHING_AND_DIFFERENTIATION_PROCEDURES_IN.10.aspx.

Yashiro, S., Gopalswamy, N., Michalek, G., St. Cyr, O.C., Plunkett, S.P., Rich, N.B., Howard, R.A.: 2004, A catalog of white light coronal mass ejections observed by the SOHO spacecraft. *Journal of Geophysical Research (Space Physics)* **109**, 7105. DOI. ADS.

Yashiro, S., Gopalswamy, N., Akiyama, S., Michalek, G., Howard, R.A.: 2005, Visibility of coronal mass ejections as a function of flare location and intensity. *Journal of Geophysical Research (Space Physics)* **110**, A12S05. DOI. ADS.

Zhang, J., Dere, K.P., Howard, R.A., Kundu, M.R., White, S.M.: 2001, On the Temporal Relationship between Coronal Mass Ejections and Flares. *Astrophys. J.* **559**, 452. DOI. ADS.

Zhang, J., Dere, K.P., Howard, R.A., Vourlidas, A.: 2004, A Study of the Kinematic Evolution of Coronal Mass Ejections. *Astrophys. J.* **604**, 420. DOI. ADS.

Zhang, W., Yan, F., Han, F., He, R., Li, E., Wu, Z., Chen, Y.: 2021, Auto Recognition of Solar Radio Bursts Using the C-DCGAN Method. *Frontiers in Physics* **9**, 646556. DOI. ADS.

Zhitnik, I.A., Bougaenko, O.I., Delaboudiniere, J.-P., Ignatiev, A.P., Korneev, V.V., Krutov, V.V., Kuzin, S.V., Lisin, D.V., Mitrofanov, A.V., Oparin, S.N., Oraevsky, V.N., Pertsov, A.A., Slemzin, V.A., Sobelman, I.I., Stepanov, A.I., Schwarz, J.: 2002, SPIRIT X-ray telescope/spectroheliometer results. In: A. Wilson (ed.) *Solar Variability: From Core to Outer Frontiers*, *ESA, Noordwijk* **SP-506**, 915. ADS.

Zhitnik, I.A., Bugaenko, O.I., Ignat'ev, A.P., Krutov, V.V., Kuzin, S.V., Mitrofanov, A.V., Oparin, S.N., Pertsov, A.A., Slemzin, V.A., Stepanov, A.I., Urnov, A.M.: 2003a, Dynamic 10 MK plasma structures observed in monochromatic full-Sun images by the SPIRIT spectroheliograph on the CORONAS-F mission. *Mon. Not. R. Astron. Soc.* **338**, 67. DOI. ADS.

Zhitnik, I., Kuzin, S., Afanas'ev, A., Bugaenko, O., Ignat'ev, A., Krutov, V., Mitrofanov, A., Oparin, S., Pertsov, A., Slemzin, V., Sukhodrev, N., Umov, A.: 2003b, XUV observations of solar corona in the spirit experiment on board the coronas-F satellite. *Adv. Space Res.* **32**, 473. DOI. ADS.

Zhu, C., Qiu, J., Liewer, P., Vourlidas, A., Spiegel, M., Hu, Q.: 2020, How Does Magnetic Reconnection Drive the Early-stage Evolution of Coronal Mass Ejections? *Astrophys. J.* **893**, 141. DOI. ADS.